Supporting Information

Precise Tailoring of Terahertz Short Pulse Semiconductor Sources with Gires–Tournois Interferometers and Active Mode-Locking

Valentino Pistore, Michael Schreiber, Anna De Vetter, Lukas Seitner, Hanond Nong, Juliette Mangeney, Jerome Tignon, Lianhe Li, Alexander Giles Davies, Edmund Harold Linfield, Christian Jirauschek, and Sukhdeep Dhillon**

1. Experimental setup

A schematic representation of the experimental setup is shown in Figure S1. The system comprises three main sections. In the first, consisting of the ultrafast optical pump and THz pulse generation, a Ti:sapphire (Ti:Sa) laser emitting ~ 100 fs pulses at a central wavelength of 800 nm is used as the optical source. The laser beam is initially split at a beam splitter into two arms. One arm is sent through a mechanical delay line and then directed to the detection section for coherent sampling. The second arm is further split: one portion is focused onto a photoconductive antenna (PCA) to generate broadband THz pulses, while the remaining portion is directed onto a fast photodiode, which serves as a reference for synchronization and signal generation. The THz pulses generated by the PCA are coupled into the QCL waveguide using a pair of off-axis parabolic mirrors to ensure efficient free-space coupling.

In the second section, namely the electronic drive and modulation circuitry, the QCL driving bias is generated and locked to the repetition rate of the Ti:Sa laser. For injection seeding, the QCL is biased just below threshold using a low-frequency (kHz-range) modulated current. A radio-frequency signal at 76 MHz, synchronized to the repetition rate of the Ti:Sa laser, is superimposed to bring the device momentarily above threshold, precisely timed to coincide with the arrival of the externally injected THz pulse. This synchronization ensures coherent seeding of the QCL emission. When active mode-locking is required, an additional RF component is injected, typically in the range of 5–20 GHz. This high-frequency modulation is generated by isolating and amplifying a suitable harmonic of the photocurrent produced by the reference photodiode. The chosen modulation frequency is selected to be close to the round-trip frequency of the QCL resonator, enabling resonant excitation of cavity modes and the formation of short THz pulses via active mode-locking.

Finally, in the third section, the emitted THz radiation from the QCL is characterized using a standard electro-optic detection scheme. This technique allows for coherent time-domain sampling of the emitted THz waveform by measuring the induced birefringence in an electro-optic crystal probed by the NIR pulses from the Ti:Sa laser.

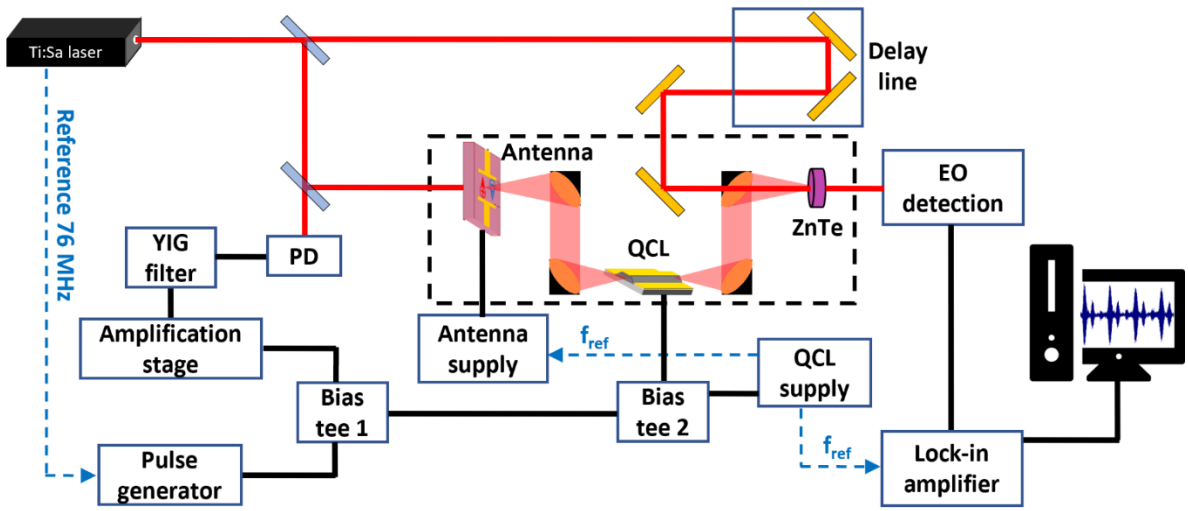


Figure S1: Schematic of the THz-TDS setup employed for the ultrafast characterization of the QCL emission.

For time-domain electro-optic sampling, the mechanical delay line was operated with a temporal step size of 60 fs for injection-seeding measurements and 90 fs for active mode-

locking scans. Due to the stringent long-term phase stability required to maintain triple electrical-optical synchronization (the sub-threshold kHz base bias, the 76 MHz seeding pulse, and the ~ 11.4 GHz active mode-locking RF modulation), acquisition windows were calibrated per measurement sequence, reaching up to ~ 2 ns. Within each comparative dataset (Figures 2, 3, 4, 5, and S4), identical temporal scanning windows were maintained to ensure identical spectral resolution across compared traces. Fast Fourier Transforms (FFTs) were calculated directly from the temporal field waveforms without zero-padding or windowing functions, and output spectra were normalized to peak intensity to facilitate direct comparison of spectral shapes and mode-locked emission bandwidths.

2. LIV and beatnote map of FC_1

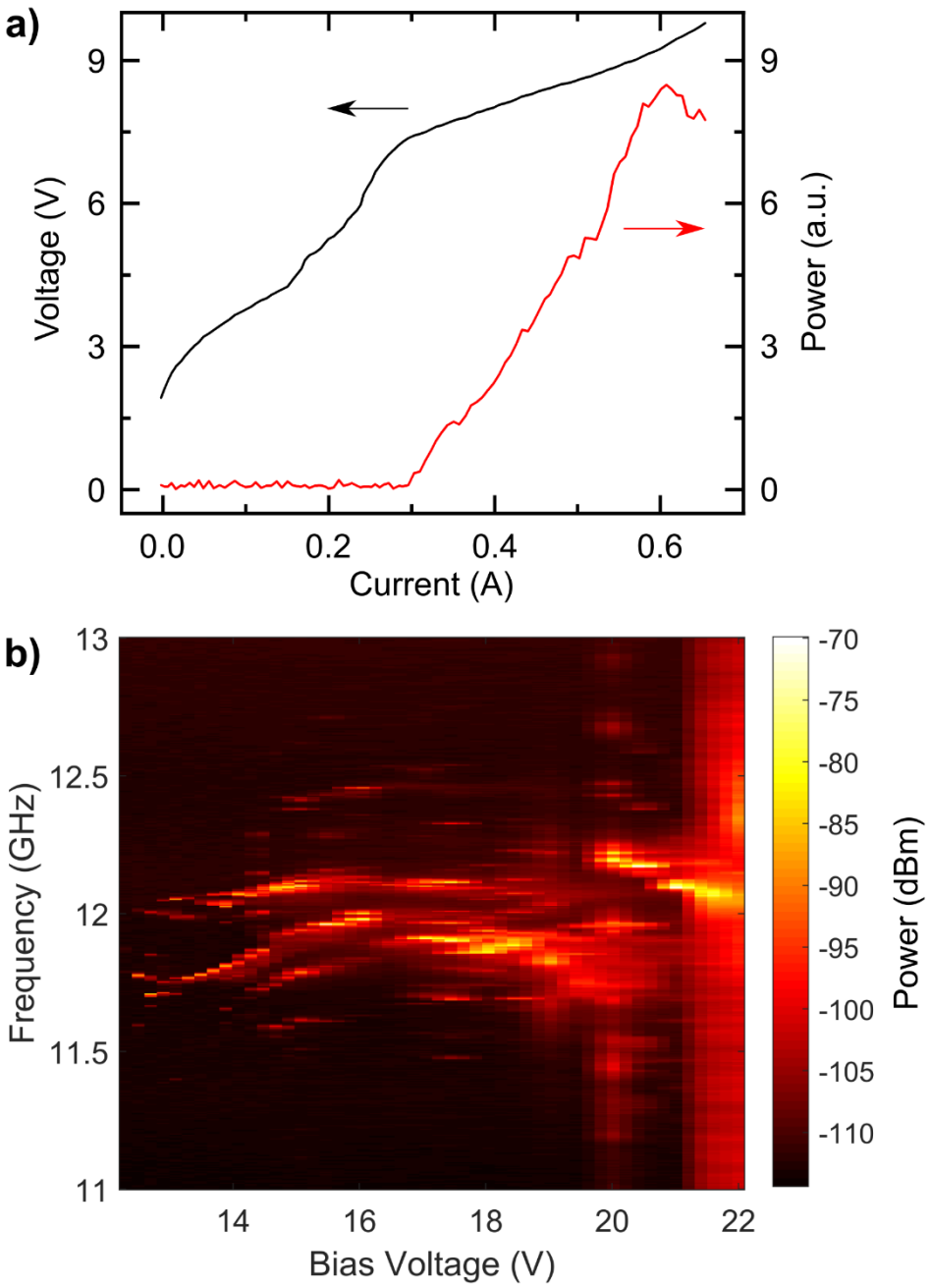


Figure S2: **a**. Light-current-voltage characteristic of FC_1 acquired at 10 K, 25 kHz current frequency, 10% duty-cycle. **b.** Beatnote map of FC_1 in the same experimental conditions as (a).

3. SEM pictures of the GTIs integrated to FC_1 and extraction of the GDD profiles

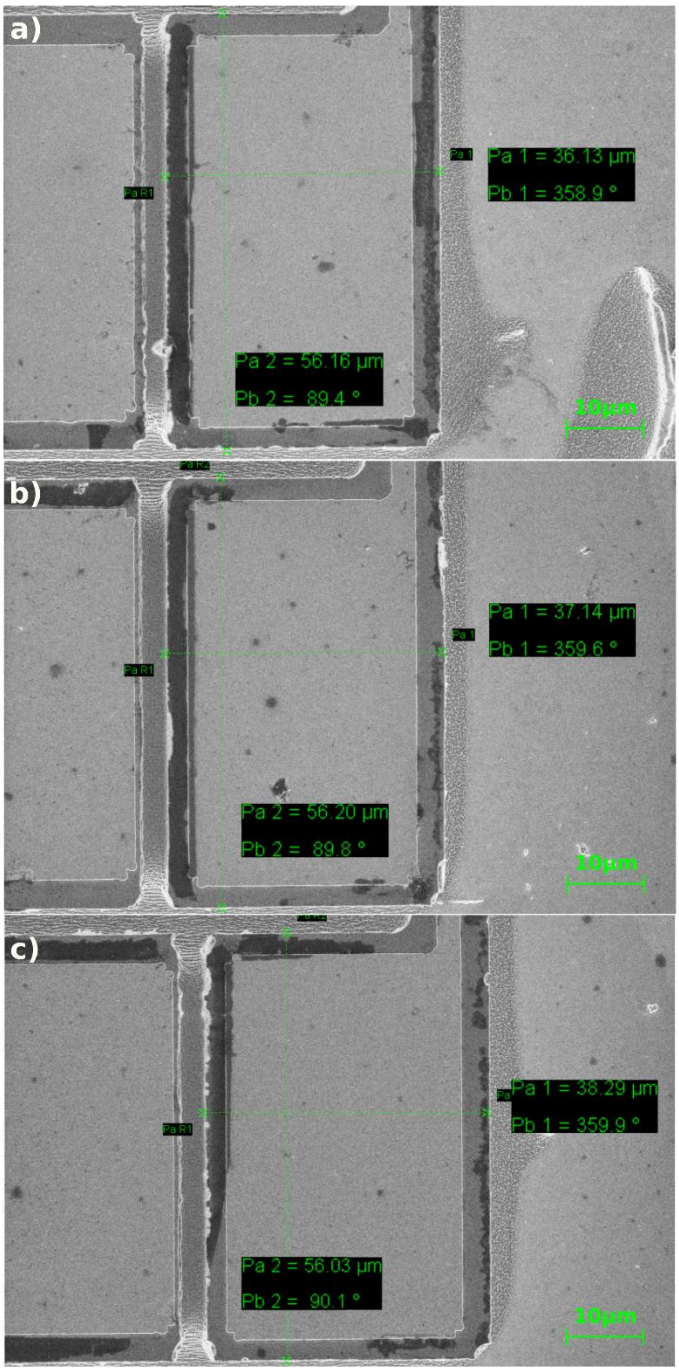


Figure S3: SEM pictures of the GTIs integrated to FC_1-36.1 (a), FC_1-37.1 (b), and FC_1-38.3 (c).

The detailed GTI structures in Figure S3 have been reconstructed in 3D COMSOL simulations to extract the precise group delay dispersion (GDD) they introduce. The simulations naturally include both waveguide and material dispersion, as the host GaAs material was modeled using a single-Lorentzian oscillator for the Reststrahlenband dielectric permittivity (model parameters in Table S1). Waveguide dispersion is fully accounted for by solving Maxwell's equations in 3D over the actual cross-sectional geometry of the double-metal structure, while

gain and loss dispersion associated with intersubband transition dynamics was neglected (transparency operating conditions are assumed).

Table S1: Material constants of GaAs employed in the COMSOL simulation

Property	Value	Unit
ε_∞	10.60	1
ε_0	12.74	1
Ω_{TO}	8.2	THz
γ	3.5	cm^{-1}

To extract the complex reflection coefficient $S_{11}(\omega) = |S_{11}|\ e^{i\phi(\omega)}$, a numeric port reference plane was positioned 5 µm inside the main QCL waveguide leading toward the gap. This setup isolates the combined gap-GTI reflection profile while decaying non-propagating higher-order evanescent modes generated at the gap interface. Acting as a matched absorber, the numeric port prevents parasitic Fabry-Perot standing waves inside the main QCL cavity from masking the GTI resonance. Standard perfectly matched layers were applied at the outer domain boundaries to absorb unguided radiative scattering from the gap.

The phase $\phi(\omega)$ of the fundamental mode was unwrapped across frequency. The GDD was calculated as the second derivative of the modal phase with respect to angular frequency:

$$GDD(\omega) = \frac{d^2\phi(\omega)}{d\omega^2} = \frac{d}{d\omega}\left(\frac{1}{v_g}\right)L_{\text{cavity}}$$

Under this convention, GDD > 0 corresponds to normal dispersion and GDD < 0 corresponds to anomalous dispersion. The 5 µm path offset introduces a minor phase shift $2\beta L_{\text{port}}$ that varies smoothly across frequency and vanishes upon taking the second derivative, ensuring that the computed GDD purely reflects the GTI, waveguide, and material dispersion.

4. Injection seeding measurements of FC_1 with the integrated GTIs

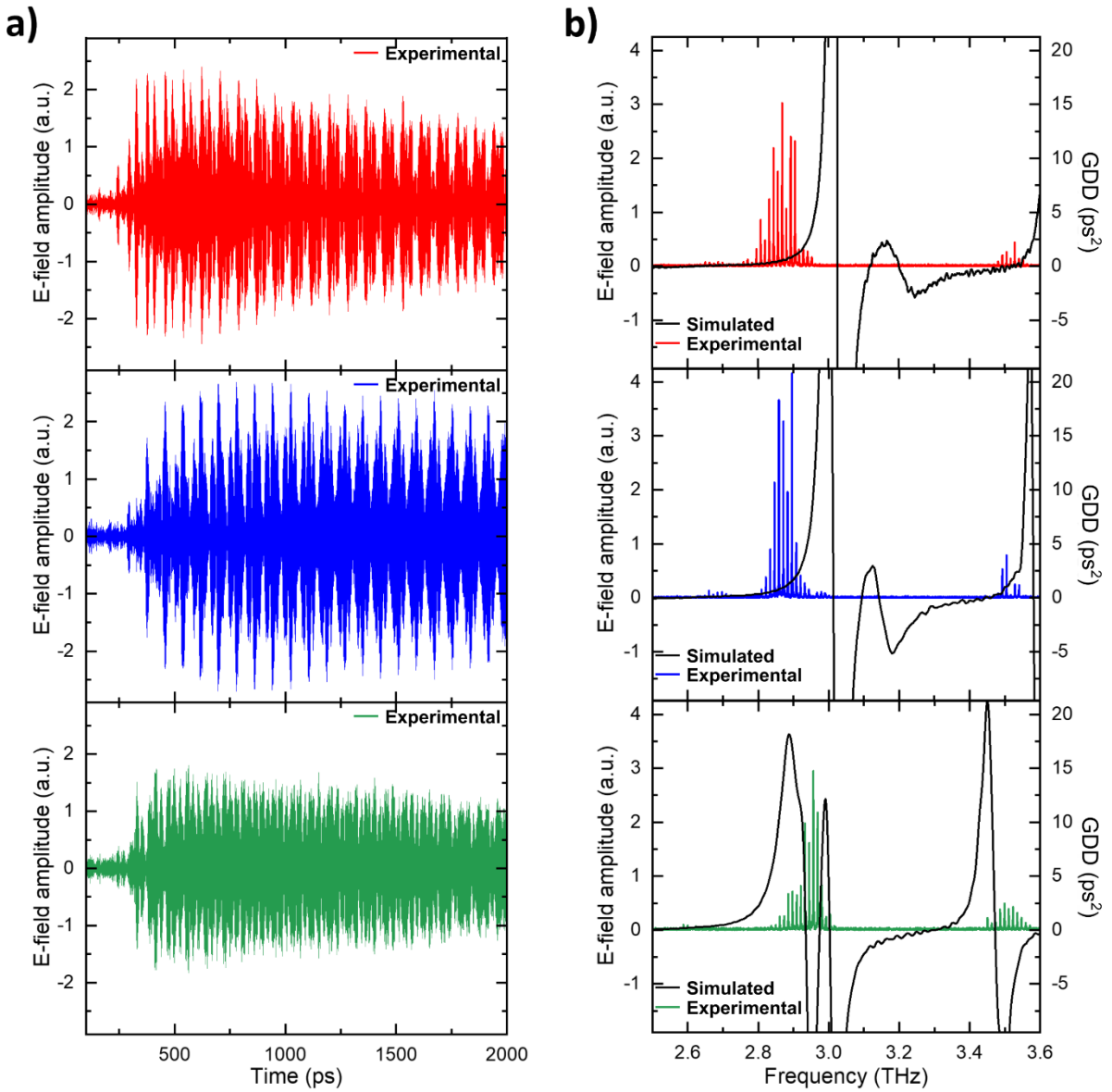


Figure S4: Experimental free-running electric field time traces (a) and FFT spectra (b) of FC_1-36.1 (top), FC_1-37.1 (middle), and FC_1-38.3 (bottom). The GDD of each GTI, as resulting from COMSOL multiphysics simulations, is reported by the black solid line.

5. Injection seeding intensity measurements and spectra of FC_2 and FC_2-66.8

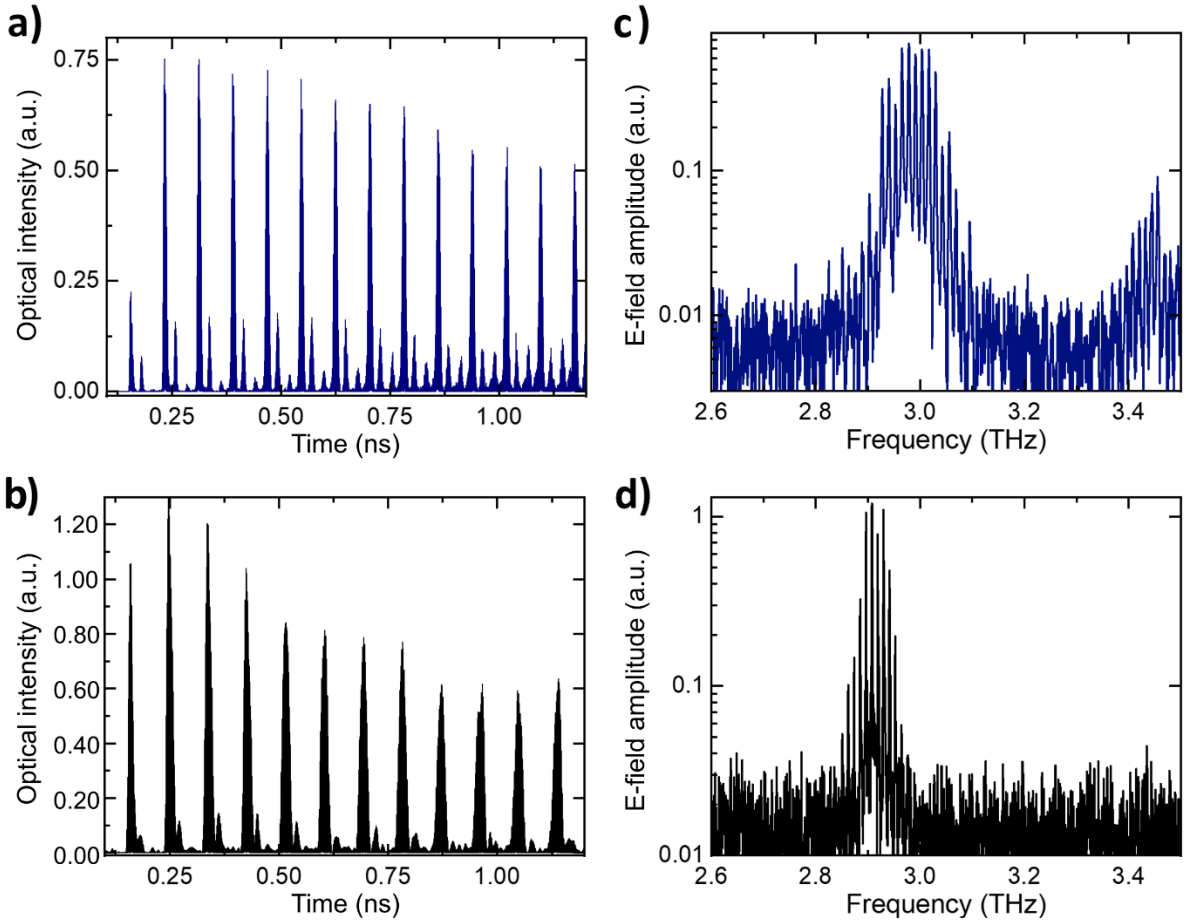


Figure S5: **a-c**. Experimental free-running optical intensity corresponding to the waveform of Figure 4a (top (a) and bottom (b)). **b-d**. Experimental electric field spectrum obtained by the FFT of the waveform of Figure 4a (top (c) and bottom (d)).

6. Mode-locking time trace and spectrum of FC_2

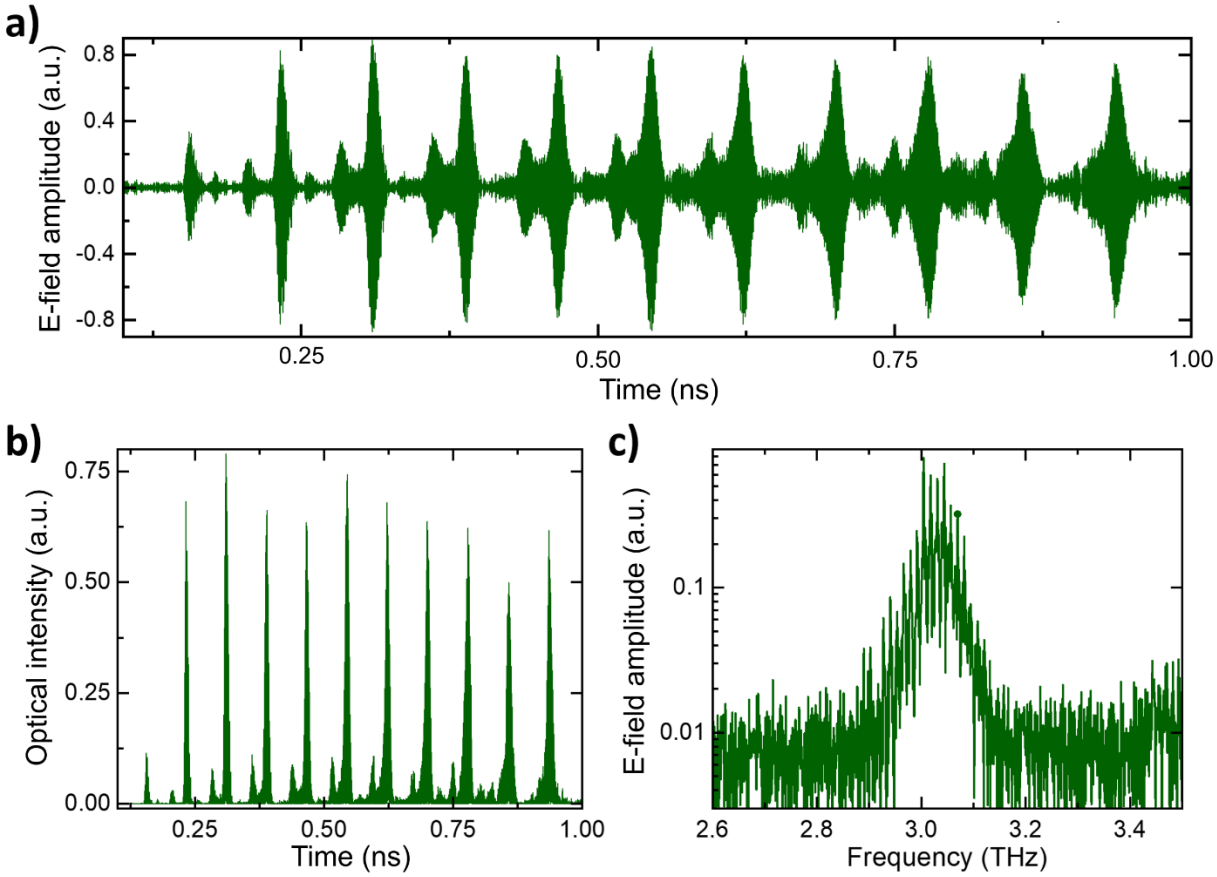


Figure S6: **a**. Experimental mode-locked electric field time trace emitted by FC_2. **b**. Optical intensity time trace associated with (a). **c**. Electric field spectrum resulting from the FFT of (a).

7. Simulation of the effect of the GTI length on the mode-locked spectra

We investigate the effect of varying the GTI length on the mode-locked spectra by simulating a simplified GTI consisting of a single region located at the right end of the simulation domain. The GTI length is scanned around the gain maximum at 3 THz. Although the resulting GDD profile does not perfectly reproduce the curves obtained from 3D COMSOL multiphysics simulations shown in Fig. 3a–c, it instead captures the standard GTI dispersion behavior. This simplification provides a clearer framework and facilitates interpretation of the results.

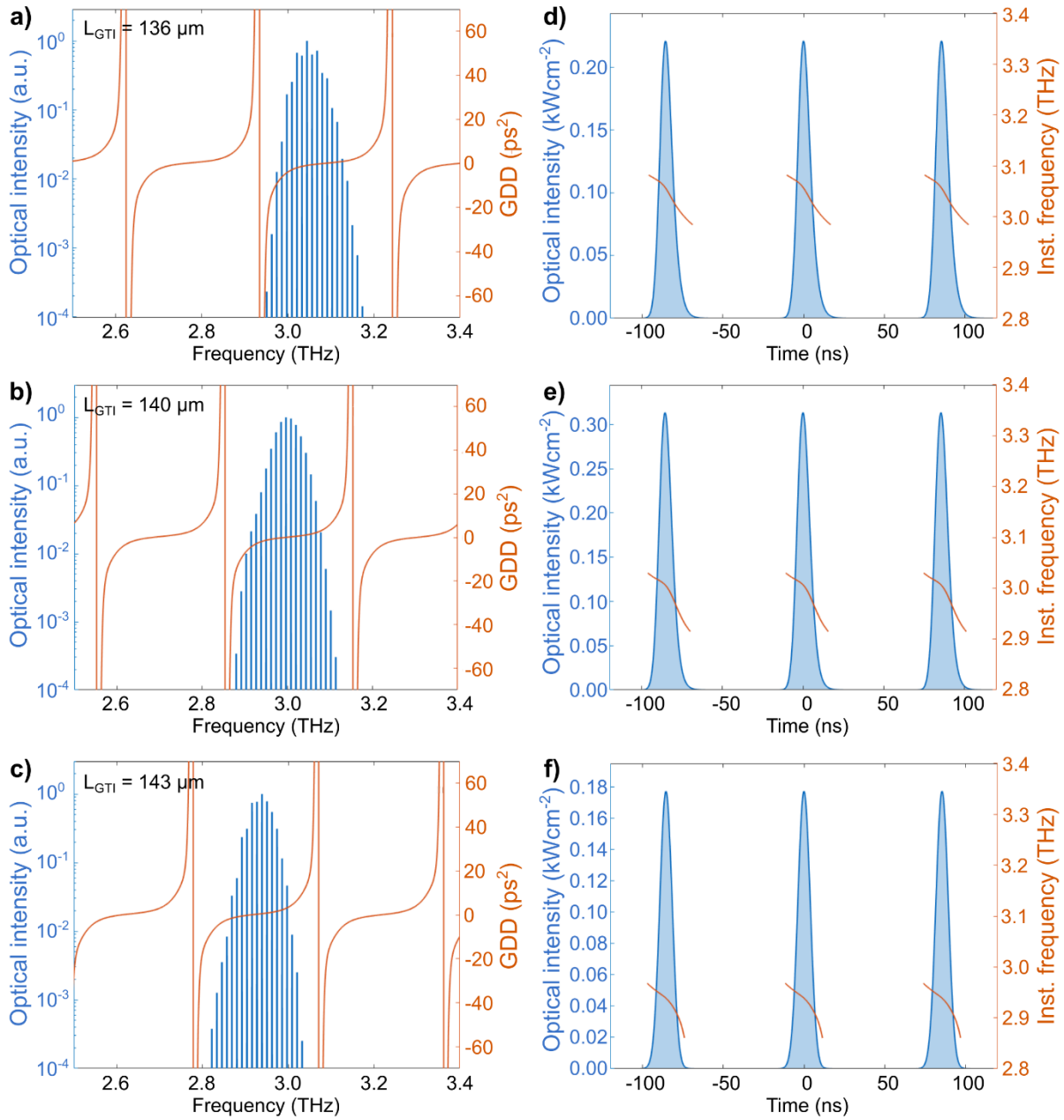


Figure S7: Simulated QCL spectra and time traces for different GTI lengths. **a–c.** Simulated GDD profiles (red) and optical intensity spectra (blue), and **d–f.** corresponding time-domain intensity traces (blue) and instantaneous frequency (red) for GTI lengths of 136 µm (a,d), 140 µm (b,e), and 143 µm (c,f).

Figure S7 presents the simulated QCL spectra (Figure S7a–c) together with the corresponding temporal traces (Figure S7d–f) for GTI lengths of 136 µm (Figure S7a,d), 140 µm (Figure S7b,e), and 143 µm (Figure S7c,f). The QCL remains mode-locked in all cases, and no parameters other than the GTI length are varied. As the GTI length increases, the low-dispersion region, where lasing occurs, shifts toward lower frequencies. Accordingly, the emission spectrum follows this shift, confirming the strong correlation between the lasing frequencies and the region of minimal GDD. A notable observation is that lasing can still occur under relatively large negative GDD, whereas positive GDD introduced by the GTI strongly suppresses lasing. This asymmetry is also consistent with the experimental spectra shown in Figure 3, highlighting that this behavior is a fundamental characteristic of THz QCLs and likely favored by positive GDD introduced by the material and gain.

Pulsed emission is observed in all temporal traces, as expected, since the spectral shape does not undergo significant qualitative changes aside from its frequency shift. However, shifting the emission away from the gain peak leads to reduced gain and consequently lower output power. This effect is evident in Figure S7d–f, where the pulse intensity decreases by approximately 30% as the spectral peak is shifted by about 100 GHz.

Table S2 summarizes the most important parameters used for the Maxwell-Bloch-based simulations in the main text and supplementary information. For a detailed description of the quantum system's parameters, we refer to Ref. [1]. The length of the cavity L is always set to 3.5 mm, whereas the GTI length L_{GTI} is varied across the manuscript and specified in the corresponding sections. As already mentioned in the main text, the GTI slit is modeled as a single point reflector, with power reflectance $R = 0.42$, while the reflectance at the facets of the QCL is assumed to be $R = 0.69$.

Table S2: Parameters for the Maxwell-Bloch-based simulations.

Parameter	Value
Cavity length L	3.5 mm
Effective refractive index n	3.6
Waveguide loss a	15 $\mathrm{cm^{-1}}$
Overlap factor Γ	0.7
Background GVD β_2	$3 \cdot 10^{-23}$ $\mathrm{s^2 m^{-1}}$
Transition frequency ω_{21}	$2\pi \cdot 2.95$ THz
Equilibrium inversion w_{eq}	0.21
Electron density $n_{3\mathrm{D}}$	$3.8 \cdot 10^{21}$ $\mathrm{m^{-3}}$
Dipole matrix element d_{21}	$e \times 6$ nm
Gain recovery time T_1	2.63 ps
Dephasing time T_2	0.167 ps

References

[1] Jirauschek, C., Riesch, M., Tzenov, P., Optoelectronic Device Simulations Based on Macroscopic Maxwell–Bloch Equations, 2019, Advanced Theory and Simulations 2, 1900018, 10.1002/adts.201900018